

Multiscale Convolutional Transformer with Center Mask Pretraining for Hyperspectral Image Classification

Sen Jia, Yifan Wang

Abstract—Hyperspectral images (HSI) not only have a broad macroscopic field of view but also contain rich spectral information, and the types of surface objects can be identified through spectral information, which is one of the main applications in hyperspectral image related research. In recent years, more and more deep learning methods have been proposed, among which convolutional neural networks (CNN) are the most influential. However, CNN-based methods are difficult to capture long-range dependencies, and also require a large amount of labeled data for model training. Besides, most of the self-supervised training methods in the field of HSI classification are based on the reconstruction of input samples, and it is difficult to achieve effective use of unlabeled samples. To address the shortcomings of CNN networks, we propose a novel multi-scale convolutional embedding module for HSI to realize effective extraction of spatial-spectral information, which can be better combined with Transformer network. In order to make more efficient use of unlabeled data, we propose a new self-supervised pretask. Similar to Mask autoencoder, but our pre-training method only masks the corresponding token of the central pixel in the encoder, and inputs the remaining token into the decoder to reconstruct the spectral information of the central pixel. Such a pretask can better model the relationship between the central feature and the domain feature, and obtain more stable training results.

Index Terms—Deep learning, mask autoencoder, transformer, hyperspectral image classification.

I. INTRODUCTION

Hyperspectral images, captured by different types of satellites, are generally composed of dozens to hundreds of bands and have the characteristics of low spatial resolution and high spectral resolution. A hyperspectral image usually provides a good overview of macroscopic surface features. The spectral information contained in the image provides the possibility to distinguish land covers, which also makes hyperspectral images widely used in various fields. This has spawned various practical applications, such as agricultural industry [1], urban planning [2], change detection [3], Lesion detection [4] and mineral detection [5], etc.

Among them, pixel-level classification of HSI is the most concerned one in the community, and its main task is to assign a class label to each pixel, which is somewhat like semantic segmentation in the computer vision (CV) field. Due to the high spectral resolution of hyperspectral images, there must be redundant bands. Principal component analysis [6] and independent component analysis [7] are widely used for redundancy elimination and have achieved good results. In the early stage of research, people mostly combine manual feature extraction methods with traditional classifiers, such

as Logistic regression [8], decision tree [9], random forest [10], and SVM [11] to classify the ground objects by spectral information. However, the imaging distance of HSI is distant and there are many inference factors in this process. Therefore, the spectral curve of different surface objects is not always easy to distinguish. This is a problem for these classification methods that take spectral information as input, and they cannot capture the patterns between features well. In recent years, deep learning methods have gradually become popular in HSI classification tasks, in which CNN-based methods are dominant. In [12], Hu et al. made a preliminary attempt of CNN models in the hyperspectral image classification task that several 1d convolutional layers are stacked to extract local spectral information, and several data augmentation method in CV field has been introduced. In [13], the authors combine 3D convolution and 2D convolution to achieve hierarchical feature learning. [14] Combining 3D convolution with 1D convolution reduces the computational cost of 3D convolution. In addition, other neural networks have also achieved good performance. Zhou et al. [15] designed two-branch Long Short-Term Memory network (LSTM) to extract spectral information and spatial information respectively. He et al. [16] proposed a pure mlp structure, proving that the mlp network still has potential. In [17], Hong et al. designed a mini batch graph neural network for HSI. It is worth mentioning that the recently very popular Transformer model has also been introduced into the field of hyperspectral classification to improve the long-range modeling capability of CNN-based model. Hu et al. [18] uses 1D convolution as an embedding layer combined with Transformer Encoder and introduces a metric learning loss. Zhong et al. [19] proposed an efficient and effective spectral-spatial transformer network and a model structure search framework.

However, deep learning models often require a large number of labeled samples as training samples, but the labeled data of HSI is limited, and large-scale sample labeling is obviously time-consuming and labor-intensive. Recently, self-supervised learning has developed vigorously. Autoregressive language modeling in GPT [20] and masked autoencoding in BERT [21] are one of the most representative methods in natural language processing (NLP). Self-supervised methods in computer vision (CV) are mainly dominated by contrastive learning methods, such as Momentum Contrast (MoCo) series [22]–[24] and SimCLR series [25], [26]. Inspired by BERT, MAE [27] leads a new hotspot of self-supervised methods in CV, and its mask-reconstruction pretask is also very instructive for related

research in HSI classification field.

In this article, a multiscale convolutional transformer is proposed for HSI classification, and a new self-supervised pretask is designed. The main contribution are listed as follows:

- According to the characteristics of hyperspectral data, a new unsupervised pre-training pretask is proposed. By the pretask of center pixel reconstructing, the model's ability to capture the relationship between the center pixel and surrounding pixels and the semantic understanding of the sample are improved.
- In conjunction with our proposed pre-training strategy, we propose a multi-scale convolutional Transformer as the backbone network. We replace the commonly used linear embedding module with a well-designed multi-scale convolutional embedding module, combined with a spectral segmentation strategy, to achieve efficient spatial-spectral feature embedding.
- A series of comparative experiments and ablation experiments demonstrate the effectiveness of our proposed pre-training method and backbone network. In particular, our proposed pre-training method can well eliminate the instability of results caused by random sampling in limited training samples scenario.

The rest of this paper is organized as follows. Our proposed method will be introduced in detail in section II. The descriptions of result analysis and comparative experiment will be provided in section III, and section IV presents the conclusions.

II. METHODOLOGY

A. Self-supervised Learning

In this section, I will introduce our proposed Multiscale convolutional Transformer (MCT) network and Center-mask pre-training pretask (CMPP). Detailed flowchart of the proposed method is in 1 and 2. The MCT network has three parts, the multiscale convolutional embedding (MCE) module, Transformer Encoder (TE), and MLP head. And CPMAE, through the mask-reconstruction process of the center pixel of the input patch, enables the backbone network to effectively model the center pixel and neighborhood pixel relationship in the self-supervised learning process.

B. Multiscale Convolutional Transformer

1) *Multiscale Convolutional Embedding*: Considering that the Vit Transformer network was originally used for RGB images, and the hyperspectral data has low spatial resolution and high spectral resolution, the original linear embedding and image segmentation strategies cannot meet the characteristics of hyperspectral data. So we propose the Multiscale Convolutional Embedding Module, which consists of a 3D spectral partition convolutional embedding (3DSPCE) branch and an independent information embedding (IIE) branch. In 3DSPCE branch, we combine the spectral partition strategy with 3D convolution. Because the spectral curves of objects often have local differences, It is difficult for a 3D convolution kernel to effectively extract the information of the entire

band. Therefore, we employ a spectral partition strategy to divide the spectrum into several subbands of equal length. 3D convolution extraction is performed for each subband, and the same convolution operation is performed twice. In addition, to unify the feature deviations generated by different spectral segments after 3D convolution, we added a 3D BatchNormalization operation. Finally, we concatenate the features, and then complete feature fusion and compression. In particular, spectral segmentation operations have a simple implementation, and the convolution function often includes a grouped convolution option.

However, only using 3D convolutional embedding can only indiscriminately extract local features of surface objects, but cannot highlight the characteristics of central features. This makes it difficult to better model the relationship between land covers. To improve this problem, we propose the independent information embedding branch, which passes each pixel of the original image through a linear embedding layer and fuses the result of the convolutional embedding by skip connections. In this way, our input sequence not only contains the information of the ground objects themselves, but also the information of the neighboring ground objects, and such multiscale embedded features are more discriminative and robust. It is worth mentioning that the convolution operation without padding will change the shape of the feature, and the shape of the IIE branch is consistent with the output of the convolution embedding branch.

2) *Transformer Encoder*: The global perception ability of CNN often needs to make the model go deeper, but HSI data is limited so it is difficult for us to stack modules as simply as a computer vision model. While, The multi-head attention module can make up for the shortcomings of CNN here, and effectively model the relationship between ground objects. A standard Transformer Encoder is shown in [?], which is mainly composed of position encoding, multi-head attention, and feedforward layers. Considering that the convolution operation itself contains position information, the position encoding is not used here, and the embedded multiscale features are directly input into the module. The definition of Scaled Dot-Product Attention and multi-head attention [28] are as follows:

$$\text{MultiHead}(Q, K, V) = \text{Concat}(\text{head}_1, \dots, \text{head}_h)W^O. \quad (1)$$

where $\text{head}_i = \text{Attention}(QW_i^Q, KW_i^K, VW_i^V).$

$$\text{Attention}(Q, K, V) = \text{softmax}\left(\frac{QK^\top}{\sqrt{d}}\right)V. \quad (2)$$

where $W_i^Q \in \mathbb{R}^{d_{models} \times d_k}, W_i^K \in \mathbb{R}^{d_{models} \times d_k}, W_i^Q \in \mathbb{R}^{d_{models} \times d_v}$ and $W^O \in \mathbb{R}^{d_{models} \times hd_v}$ are parameter matrices. Q , K and V are the learnable weight matrices. d_{model} and d_v are the dimension of input embedding and K . d_k is the dimension of Q and K . Finally, we add an average pooling layer to achieve feature compression and de-redundancy, and output the classification results through the three-layer MLP head.

C. Center-mask Pre-training Pretask

Today, most hyperspectral image classification methods are patch-based, that is, the input of the model is not only the

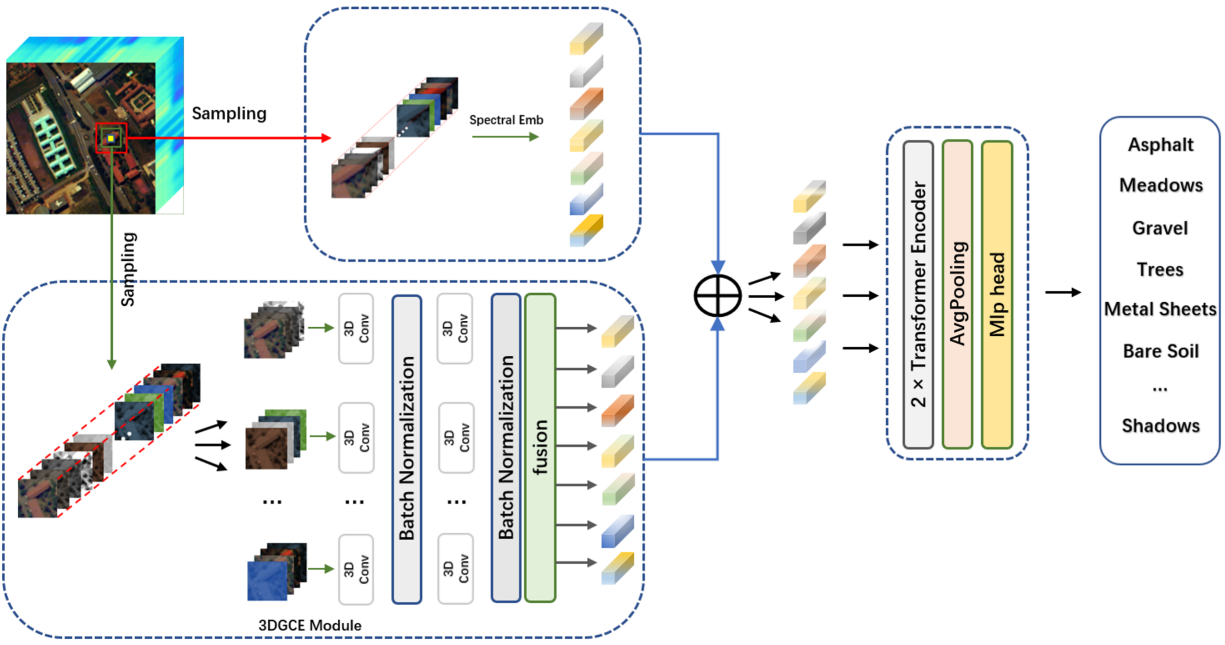


Fig. 1. Architecture of the proposed multiscale convolutional transformer for hyperspectral image classification

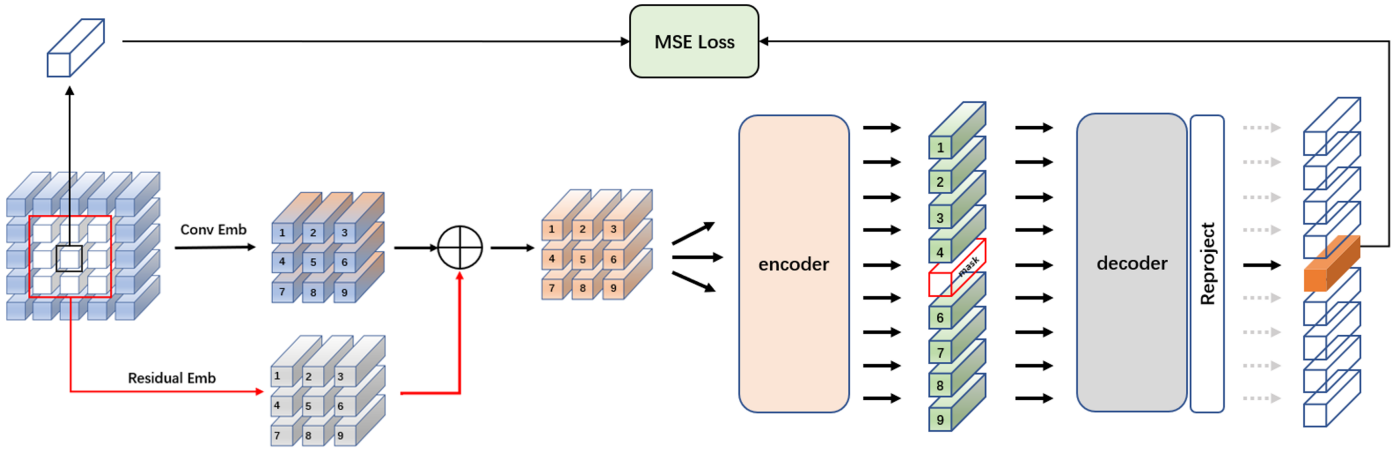


Fig. 2. Architecture of the proposed center mask pretraining pretask

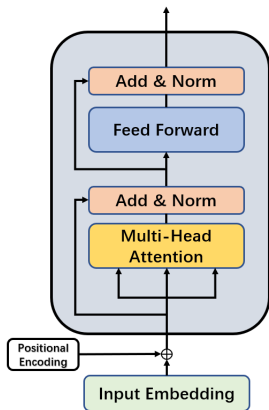


Fig. 3. Detail structure of a standard Transformer Encoder

spectral curve of center pixel, but also its neighbor region, which are generally square areas, so that the input samples can be more distinctive. Inspired by the form of the HSI sample, we propose the Center Mask (CM) Pre-training pretask, which is similar to MAE and adopts an asymmetric structure but is simpler and easier to implement.

The flowchart of CM Pre-training pretask is shown in 2. The Encoder is MCT network (with the mlp header removed). The decoder consists of two layers of standard Transformer Encoders, which are only used in the pre-training process. Given an input sample X , center pixel vector V_c , The latent representation of the input sample is E (embedded by the MCT module). Unlike self-supervised pre-training in CV field, RGB images cannot directly find areas that need to be focused, but the neighborhood areas of HSI samples are to enrich the spatial features of the central pixel. In this way, our mask

target can select the most important part of the input, that is, the center pixel. Therefore, we use a learnable vector \hat{V}_l to replace the representation corresponding to the center pixel without disturbing the order of the embedding sequence. Then, the embedded sequence is input into the decoder, and the pixel-level reconstruction is performed by the MLP head to obtain the reconstruction result \hat{V}_l of the center pixel. The target of the CM pre-training task is to reconstruct the center pixel as efficiently as possible, so that the encoder can better learn the relationship between the center pixel and the neighbor pixels without labels. The reconstruction target can be formulated as:

$$\mathcal{T}(V_c, \hat{V}_l) = \min |V_c - \hat{V}_l|_2 \quad (3)$$

where \mathcal{T} is the similarity function. In the deep learning framework, Func \mathcal{T} is equivalent to the mean squared error (MSE) loss function.

III. EXPERIMENT

To fully evaluate our proposed pre-training method and backbone network, we conduct comparative experiments and ablation experiments on two public datasets, Salinas and Yellow River Estuary (YRE). The false-color image and ground-truth are shown in Fig. 3 and Fig. 4 and The detailed information and The portion of the training set and test set are shown in the table. We use three metrics to evaluate the classification results, overall accuracy (OA), classwise average accuracy (AA), and kappa coefficient.

A. Datasets Description

1) *Salinas Dataset*: The salinas dataset, collected by the AVIRS sensor in the Salinas Valley, USA, has an image resolution of 512×217 and a spatial resolution of 3.7 meters. After noise band removal, 204 bands are remaining. There are 16 kinds of ground objects in the dataset, with a total of 56,975 samples that can be used for pixel-level classification.

2) *YRE Dataset*: YRE dataset is a large scene dataset captured by the Gaofen-5 satellite in the Yellow River Estuary region of Shandong Province, China. Its height and width are 1400, and the spatial resolution of each pixel is 30m, leaving 180 bands after removing noise bands. The surface objects are mainly wetland vegetation, there are 20 kinds of objects and the total number of labeled samples is 77,937.

B. Comparative Experiment

To demonstrate the superiority of our proposed method, we select six state-of-the-art methods on two public datasets, Salinas and YRE, including five CNN methods and one classical Transformer network. They are CNNHSI [29], SPRN [30], FC3D [31], HybridSN [32], TwoCNN [33] and Vision Transformers (ViT) [34]. Among them, several methods based on 2DCNN are distinguished in the size of the convolution kernel and the structure design. CNNHSI stacks several 2-D Convolution layer with 1×1 kernel size. SPRN adopts spectral partition (SP) operation and applies several parallel 3×3 convolutions. TwoCNN is a dual-branch CNN with a 2DCNN and a 1DCNN to extract spatial information

TABLE I
LAND COVER CLASSES OF THE SALINAS DATASET, WITH THE STANDARD TRAINING AND TESTING SETS FOR EACH CLASS.

Class	Class Name	Training	Testing
1	Broccoli green weeds 1	5	2004
2	Broccoli green weeds 2	5	3721
3	Fallow	5	1971
4	Fallow rough plow	5	1389
5	Fallow smooth	5	2673
6	Stubble	5	3954
7	Celery	5	3574
8	Grapes untrained	5	11266
9	Soil vinyard develop	5	6198
10	Corn senesced green weeds	5	3273
11	Lettuce romaine 4wk	5	1063
12	Lettuce romaine 5wk	5	1922
13	Lettuce romaine 6wk	5	911
14	Lettuce romaine 7wk	5	1065
15	Vinyard untrained	5	7263
16	Vinyard vertical trellis	5	1802
	Total	80	54129

TABLE II
LAND COVER CLASSES OF THE YRE DATASET, WITH THE STANDARD TRAINING AND TESTING SETS FOR EACH CLASS.

Class	Class Name	Training	Testing
1	Building	10	523
2	River	10	5366
3	Salt Marsh	10	4985
4	Shallow Sea	10	17540
5	Deep Sea	10	18667
6	Intertidal Saltwater Marsh	10	2333
7	Tidal Flat	10	1782
8	Pond	10	1777
9	Sorghum	10	636
10	Corn	10	1499
11	Lotus Root	10	2709
12	Aquaculture	10	8009
13	Rice	10	5498
14	Tamarix Chinensis	10	1210
15	Freshwater Herbaceous Marsh	10	1407
16	Suaeda Salsa	10	864
17	Spartina Alterniflora	10	570
18	Reed	10	1960
19	Floodplain	10	337
20	Locus	10	65
	Total	200	77737

and spectral information respectively. FC3D is a pure 3DCNN network, and HybridSN uses 3D convolution and 2D con-

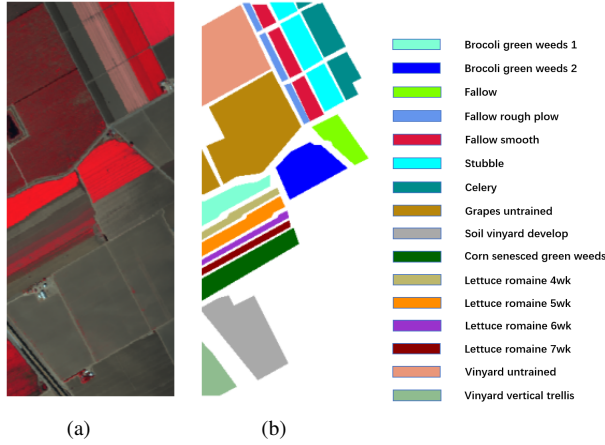


Fig. 4. (a) False-color image and (b) Ground-truth map of the Salinas dataset.

volution successively for hierarchical feature extraction. Vit takes each pixel vector in the patch as the input. The model structure and parameter settings of the comparison methods comply with open source codes or corresponding papers.

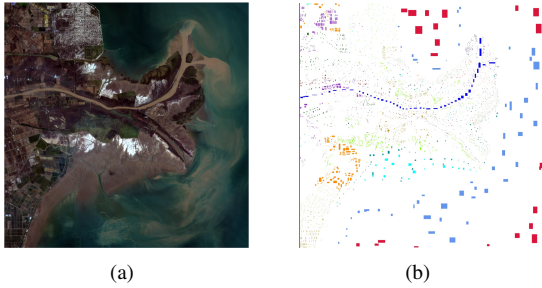


Fig. 5. (a) False-color image and (b) Ground-truth map of the YRE dataset.

The results of the comparative experiments are shown in III and IV. It can be seen that our method has obtained obvious advantages, and achieved the best or second-best results in classification accuracy in each class, which reflects the superiority and robustness of our method. Under the setting of limited training samples, CNNHSI also achieves excellent classification results due to its lightweight network structure. The performance of SPRN is also good, which benefits from the design of the spectral partition operation. Limited by the large model size, HybridSN, FC3D, and TwoCNN failed to obtain superior classification results. The Transformer structure is often data-hungry, and it is difficult to directly compete with the CNN structure in small sample scenarios. Therefore, this directly proves the necessity of a well-designed embedding layer for HSI in Transformer network. So, we designed a dual-branch convolution embedding module in a targeted manner, combined with the CM pre-training strategy, to further improve the performance of the model in the case of small samples, and realize the effective use of unlabeled samples. In addition, all the methods can't discriminate the Vineyard untrained class well, which may be limited by the large variability of this land cover, which is also a problem we need to solve in the future. The classification results of each method on the YRE

TABLE III
CLASSIFICATION ACCURACY (%) AND KAPPA MEASURE FOR THE SALINAS DATASET

Class	Vit	HybridSN	FC3D	CNNHSI	TwoCNN	SPRN	MCT
1	100.00	99.93	99.95	93.64	93.44	99.75	100.00
2	99.54	98.31	92.92	79.30	89.86	96.17	99.61
3	99.98	97.04	97.84	84.62	90.63	84.85	99.99
4	95.68	93.18	96.66	99.40	97.45	92.80	98.91
5	96.04	98.08	86.54	77.31	95.23	90.10	95.51
6	99.76	98.46	94.08	98.45	99.74	99.69	99.93
7	99.99	99.76	99.78	99.13	100.00	97.84	100.00
8	78.79	59.81	53.82	65.56	74.59	64.14	84.08
9	98.22	96.84	95.46	94.70	99.67	95.91	99.57
10	92.63	93.33	90.32	46.59	95.17	82.94	95.92
11	98.42	97.65	89.21	90.40	95.71	91.56	99.94
12	97.60	94.88	91.28	97.85	99.20	92.54	98.72
13	85.03	84.63	87.82	99.19	99.28	88.80	98.57
14	97.60	98.97	92.99	92.94	96.39	90.14	99.58
15	68.61	71.60	65.73	40.12	66.80	72.82	70.49
16	99.00	79.97	88.53	82.69	96.38	97.37	99.32
OA (%)	89.90	85.24	81.65	76.41	87.99	84.80	92.04
AA (%)	94.18	91.40	88.93	83.87	93.10	89.84	96.26
κ	88.77	83.70	79.78	73.74	86.65	83.17	91.13

dataset are similar to the Salinas dataset, but the YRE dataset is a large scene dataset, and the classification task is more difficult, so the classification performance of each method is slightly lower than that on the Salinas dataset. It is worth mentioning that TwoCNN achieves good classification results, which may benefit from its spectral feature extraction branch. The classification results of each method on the YRE dataset are similar to the Salinas dataset, but the YRE dataset is a large scene dataset, and the classification task is more complicated. So, the classification performance of each method is slightly lower than that of the Salinas dataset. It is worth mentioning that TwoCNN achieves good classification results, which may benefit from its spectral feature extraction branch.

Besides, considering that the YRE dataset did not completely label all samples, to fully display the classification performance between comparison methods, We use partial prediction and full prediction in the generation of classification results for the Salinas and YRE datasets, respectively. That is, for the Salinas dataset, we only visualize labeled samples, and for YRE, we make predictions for the entire dataset. The classification map of Salinas is shown in [Figure]. It can be seen that the classification results of our method are almost consistent with the Groundtruth in most classes, while other methods have different numbers of classification errors in almost every land covers. This intuitively reflects the stability of our method. The classification map of YRE is shown in [Figure]. Similarly, our proposed method restores the distribution of surface objects well, but there is a smearing phenomenon. In contrast, although the classification accuracy

TABLE IV
CLASSIFICATION ACCURACY (%) AND KAPPA MEASURE FOR
THE YRE DATASET

Class	Vit	HybridSN	FC3D	CNNHSI	TwoCNN	SPRN	MCT
1	49.78	82.35	78.84	92.16	70.48	86.46	85.58
2	95.45	100.00	99.93	99.12	99.96	99.90	98.45
3	55.45	61.34	72.20	75.74	85.93	79.80	87.40
4	78.22	71.04	72.78	83.22	90.44	89.67	93.67
5	85.89	76.74	90.49	86.98	97.59	97.81	98.26
6	79.48	81.77	83.37	85.30	82.65	82.52	86.87
7	56.38	51.53	57.30	57.89	63.63	57.44	60.04
8	73.16	73.94	73.68	78.41	60.17	84.03	80.34
9	75.10	85.90	86.11	86.67	82.70	86.26	88.74
10	57.06	70.82	62.15	90.93	72.22	88.46	90.65
11	63.65	82.55	83.38	89.97	75.71	79.79	90.80
12	72.82	76.36	79.69	77.93	73.76	77.35	83.95
13	71.27	87.47	84.49	92.27	87.79	90.88	91.26
14	67.11	75.32	76.50	88.38	88.63	89.95	83.75
15	59.32	64.65	74.65	85.73	96.32	89.40	66.87
16	74.27	93.02	89.89	93.73	92.20	94.84	96.19
17	81.29	93.98	89.47	96.67	93.72	99.26	98.40
18	44.74	58.11	62.74	65.66	67.59	68.96	67.95
19	60.53	82.89	68.25	88.61	68.84	80.06	82.67
20	87.69	91.28	71.79	87.69	64.00	86.77	87.69
OA (%)	75.58	76.14	80.84	84.61	87.45	88.58	90.72
AA (%)	69.43	78.05	77.88	85.15	80.72	85.48	85.98
κ	71.87	72.96	78.09	82.30	85.48	86.77	89.26

of SPRN is slightly lower, its classification map appears smoother. This is also the direction of improvement that we need in the future.

C. Ablation Study

In this section we conduct comprehensive ablation experiments on the multi-scale convolutional embedding module and the center mask-reconstruction pre-training pretask (PTP). The experimental results are shown in table V. The experimental results compared with the Vit model can intuitively demonstrate the effectiveness of our proposed MCE module. On this basis, we further demonstrate the effectiveness of the IIE branch in the MCE module. For the convenience of description, we name the MCT model after removing the IIE branch as 3DCT. The experimental results on the Salinas and YRE datasets show that the accuracy of MCT is 0.47% and 2.12% higher than that of 3DCT, respectively.

Finally, various ablation experiments are performed on our proposed pre-training pretask. The experimental results on the Salinas and YRE datasets show that the model fine-tuned on pre-trained model (PTM) outperforms the model without pre-training by 2.97% and 2.2%, respectively. In addition, we do additional experiments on the 3DSPCT model, fine-tuning 3DSPCT on PTM of MCT (removing the parameters of the IIE module). The experimental results prove that no

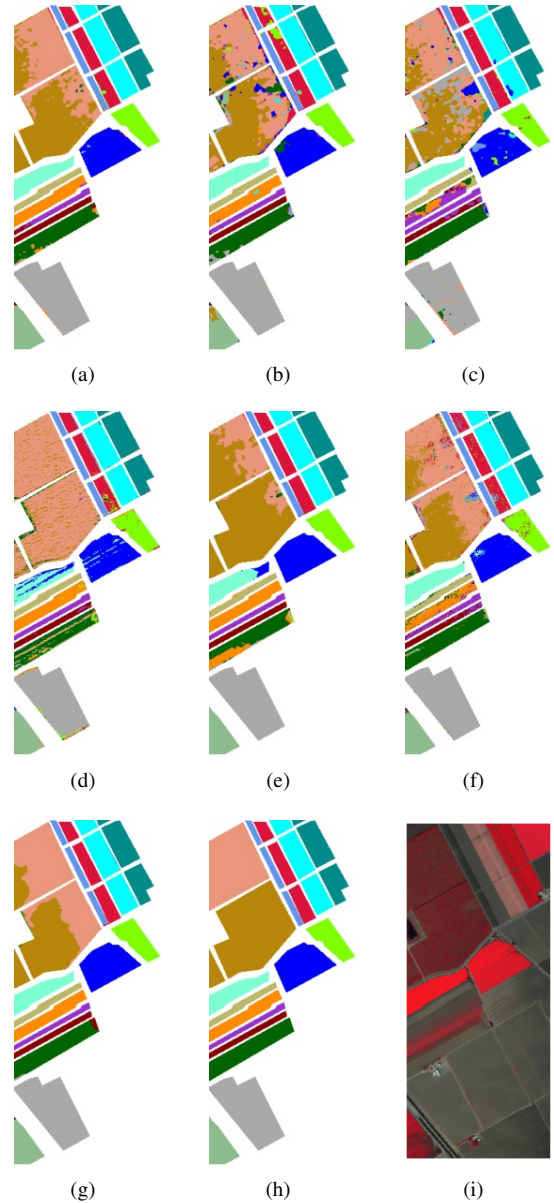


Fig. 6. Salinas dataset. Classification maps obtained by (a) CNNHSI(89.90%), (b) 3D-2D-CNN(85.24%), (c) 3D-CNN(81.65%), (d) Two-CNN(76.41%), (e) SPRN(87.99%), (f) Vit(84.80%), (g) Ours(92.04%),and (h) Ground-truth and (i) False-color image

matter fine-tuning on PTM of 3DSPCT or MCT, competitive experimental results can be obtained. This undoubtedly proves the superiority and robustness of our pre-training pretask.

IV. CONCLUSION

In this article, we propose a reconstruction-based pre-training pretask and lightweight backbone network for HSI. We creatively propose a multi-scale convolutional embedding module to extract spatial spectral information at different scales with 3D convolution and linear embedding using spectral segmentation strategy, respectively, to obtain more discriminative embeddings. The Transformer module is used to model the global relationship between surface object representations. Additionally, for few-shot scenarios, we propose a new

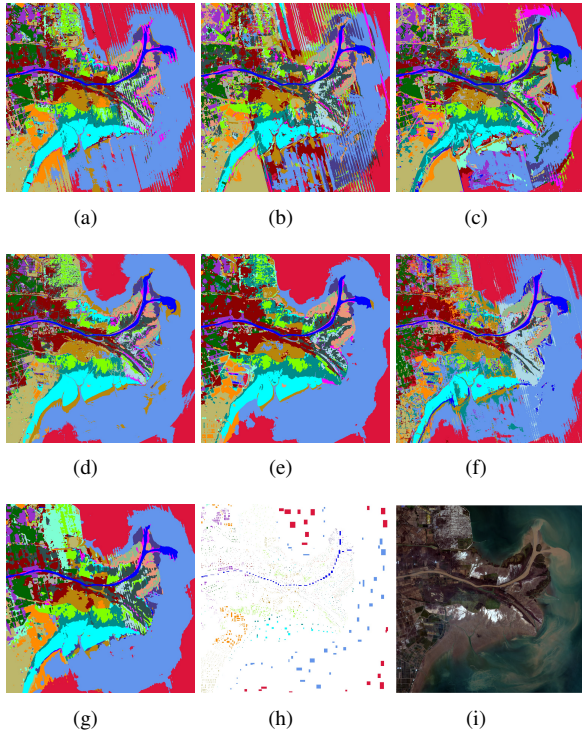


Fig. 7. YRE dataset. Classification maps obtained by (a) CNNHSI(89.90%), (b) 3D-2D-CNN(85.24%), (c) 3D-CNN(81.65%), (d) Two-CNN(76.41%), (e) SPRN(87.99%), (f) Vit(84.80%), (g) Ours(92.04%), (h) Ground-truth, and (j) False-color image

TABLE V
ABLATION STUDY RESULTS TOWARD THE MCE MODULE AND
CMR PRETRAINING PRETASK ON SALINAS AND YRE
DATASETS

Dataset	Module		Pretrain Model		Metric		
	3DSPCE	IIE	full	partial	OA (%)	AA (%)	κ
Salinas	✓	✓	✗	✗	89.12	95.03	87.92
Salinas	✓	✗	✗	✗	88.60	85.42	86.46
Salinas	✓	✓	✓	✗	92.04	96.26	91.13
Salinas	✓	✗	✓	✗	89.99	95.40	88.87
Salinas	✓	✗	✗	✓	89.66	95.85	88.54
YRE	✓	✓	✗	✗	88.64	85.34	86.88
YRE	✓	✗	✗	✗	86.24	82.19	84.15
YRE	✓	✓	✓	✗	90.72	85.98	89.26
YRE	✓	✗	✓	✗	89.01	84.11	87.30
YRE	✓	✗	✗	✓	90.51	86.01	89.01

unsupervised pre-training pretask suitable for hyperspectral classification tasks. Through the mask and reconstruction process of the token generated based on the central pixel vector, the model can better learn the relationship between the neighboring surface objects and the central surface object during the pre-training process, and can provide more stable experimental results and model performance. We conducted a series of comparative experiments and ablation experiments on two public datasets, Salinas and YRE, to demonstrate the effectiveness and superiority of our proposed method.

REFERENCES

- [1] R. N. Sahoo, S. Ray, and K. Manjunath, "Hyperspectral remote sensing of agriculture," *Current Science*, pp. 848–859, 2015.
- [2] C. Weber, R. Aguejidad, X. Briottet, J. Avala, S. Fabre, J. Demuyneck, E. Zenou, Y. Deville, M. S. Karoui, F. Z. Benhalouche, *et al.*, "Hyperspectral imagery for environmental urban planning," in *IGARSS 2018-2018 IEEE International Geoscience and Remote Sensing Symposium*, pp. 1628–1631, IEEE, 2018.
- [3] S. Liu, D. Marinelli, L. Bruzzone, and F. Bovolo, "A review of change detection in multitemporal hyperspectral images: Current techniques, applications, and challenges," *IEEE Geoscience and Remote Sensing Magazine*, vol. 7, no. 2, pp. 140–158, 2019.
- [4] S. S. Basha, S. Ghosh, K. K. Babu, S. R. Dubey, V. Pulabaigari, and S. Mukherjee, "Rccnet:an efficient convolutional neural network for histological routine colon cancer nuclei classification," in *2018 15th International Conference on Control, Automation, Robotics and Vision (ICARCV)*, pp. 1222–1227, IEEE, 2018.
- [5] E. Bedini, "The use of hyperspectral remote sensing for mineral exploration: A review," *Journal of Hyperspectral Remote Sensing*, vol. 7, no. 4, pp. 189–211, 2017.
- [6] M. D. Farrell and R. M. Mersereau, "On the impact of pca dimension reduction for hyperspectral detection of difficult targets," *IEEE Geoscience and Remote Sensing Letters*, vol. 2, no. 2, pp. 192–195, 2005.
- [7] S. Moussaoui, H. Hauksdottir, F. Schmidt, C. Jutten, J. Chanussot, D. Brie, S. Douté, and J. A. Benediktsson, "On the decomposition of mars hyperspectral data by ica and bayesian positive source separation," *Neurocomputing*, vol. 71, no. 10-12, pp. 2194–2208, 2008.
- [8] Y. Qian, M. Ye, and J. Zhou, "Hyperspectral image classification based on structured sparse logistic regression and three-dimensional wavelet texture features," *IEEE Transactions on Geoscience and Remote Sensing*, vol. 51, no. 4, pp. 2276–2291, 2012.
- [9] S. Kuching, "The performance of maximum likelihood, spectral angle mapper, neural network and decision tree classifiers in hyperspectral image analysis," *Journal of Computer Science*, vol. 3, no. 6, pp. 419–423, 2007.
- [10] J. Xia, P. Ghamisi, N. Yokoya, and A. Iwasaki, "Random forest ensembles and extended multiextinction profiles for hyperspectral image classification," *IEEE Transactions on Geoscience and Remote Sensing*, vol. 56, no. 1, pp. 202–216, 2017.
- [11] M. Chi, R. Feng, and L. Bruzzone, "Classification of hyperspectral remote-sensing data with primal svm for small-sized training dataset problem," *Advances in space research*, vol. 41, no. 11, pp. 1793–1799, 2008.
- [12] W. Hu, Y. Huang, L. Wei, F. Zhang, and H. Li, "Deep convolutional neural networks for hyperspectral image classification," *Journal of Sensors*, vol. 2015, 2015.
- [13] S. K. Roy, G. Krishna, S. R. Dubey, and B. B. Chaudhuri, "Hybridsn: Exploring 3-d-2-d cnn feature hierarchy for hyperspectral image classification," *IEEE Geoscience and Remote Sensing Letters*, vol. 17, no. 2, pp. 277–281, 2019.
- [14] A. B. Hamida, A. Benoit, P. Lambert, and C. B. Amar, "3-d deep learning approach for remote sensing image classification," *IEEE Transactions on geoscience and remote sensing*, vol. 56, no. 8, pp. 4420–4434, 2018.
- [15] F. Zhou, R. Hang, Q. Liu, and X. Yuan, "Hyperspectral image classification using spectral-spatial lstms," *Neurocomputing*, vol. 328, pp. 39–47, 2019.
- [16] X. He and Y. Chen, "Modifications of the multi-layer perceptron for hyperspectral image classification," *Remote Sensing*, vol. 13, no. 17, p. 3547, 2021.
- [17] D. Hong, L. Gao, J. Yao, B. Zhang, A. Plaza, and J. Chanussot, "Graph convolutional networks for hyperspectral image classification," *IEEE Transactions on Geoscience and Remote Sensing*, vol. 59, no. 7, pp. 5966–5978, 2020.
- [18] X. Hu, W. Yang, H. Wen, Y. Liu, and Y. Peng, "A lightweight 1-d convolution augmented transformer with metric learning for hyperspectral image classification," *Sensors*, vol. 21, no. 5, p. 1751, 2021.
- [19] Z. Zhong, Y. Li, L. Ma, J. Li, and W.-S. Zheng, "Spectral-spatial transformer network for hyperspectral image classification: A factorized architecture search framework," *IEEE Transactions on Geoscience and Remote Sensing*, 2021.
- [20] A. Radford, K. Narasimhan, T. Salimans, and I. Sutskever, "Improving language understanding by generative pre-training," 2018.
- [21] J. Devlin, M.-W. Chang, K. Lee, and K. Toutanova, "Bert: Pre-training of deep bidirectional transformers for language understanding," *arXiv preprint arXiv:1810.04805*, 2018.

- [22] K. He, H. Fan, Y. Wu, S. Xie, and R. Girshick, "Momentum contrast for unsupervised visual representation learning," in *Proceedings of the IEEE/CVF conference on computer vision and pattern recognition*, pp. 9729–9738, 2020.
- [23] X. Chen, H. Fan, R. Girshick, and K. He, "Improved baselines with momentum contrastive learning," *arXiv preprint arXiv:2003.04297*, 2020.
- [24] X. Chen, S. Xie, and K. He, "An empirical study of training self-supervised visual transformers," *arXiv e-prints*, pp. arXiv–2104, 2021.
- [25] T. Chen, S. Kornblith, M. Norouzi, and G. Hinton, "A simple framework for contrastive learning of visual representations," in *International conference on machine learning*, pp. 1597–1607, PMLR, 2020.
- [26] T. Chen, S. Kornblith, K. Swersky, M. Norouzi, and G. E. Hinton, "Big self-supervised models are strong semi-supervised learners," *Advances in neural information processing systems*, vol. 33, pp. 22243–22255, 2020.
- [27] K. He, X. Chen, S. Xie, Y. Li, P. Dollár, and R. Girshick, "Masked autoencoders are scalable vision learners," *arXiv preprint arXiv:2111.06377*, 2021.
- [28] A. Vaswani, N. Shazeer, N. Parmar, J. Uszkoreit, L. Jones, A. N. Gomez, Ł. Kaiser, and I. Polosukhin, "Attention is all you need," *Advances in neural information processing systems*, vol. 30, 2017.
- [29] S. Yu, S. Jia, and C. Xu, "Convolutional neural networks for hyperspectral image classification," *Neurocomputing*, vol. 219, pp. 88–98, 2017.
- [30] X. Zhang, S. Shang, X. Tang, J. Feng, and L. Jiao, "Spectral partitioning residual network with spatial attention mechanism for hyperspectral image classification," *IEEE transactions on geoscience and remote sensing*, 2021.
- [31] M. Ahmad, A. M. Khan, M. Mazzara, S. Distefano, M. Ali, and M. S. Sarfraz, "A fast and compact 3-d cnn for hyperspectral image classification," *IEEE Geoscience and Remote Sensing Letters*, 2020.
- [32] S. K. Roy, G. Krishna, S. R. Dubey, and B. B. Chaudhuri, "Hybridsn: Exploring 3-d–2-d cnn feature hierarchy for hyperspectral image classification," *IEEE Geoscience and Remote Sensing Letters*, vol. 17, no. 2, pp. 277–281, 2020.
- [33] J. Yang, Y.-Q. Zhao, and J. C.-W. Chan, "Learning and transferring deep joint spectral–spatial features for hyperspectral classification," *IEEE Transactions on Geoscience and Remote Sensing*, vol. 55, no. 8, pp. 4729–4742, 2017.
- [34] A. Dosovitskiy, L. Beyer, A. Kolesnikov, D. Weissenborn, X. Zhai, T. Unterthiner, M. Dehghani, M. Minderer, G. Heigold, S. Gelly, *et al.*, "An image is worth 16x16 words: Transformers for image recognition at scale," *arXiv preprint arXiv:2010.11929*, 2020.